# Preparation of TiO$_2$-supported Au nanoparticle catalysts from a Au$_{13}$ cluster precursor: Ligand removal using ozone exposure versus a rapid thermal treatment

Laurent D. Menard [a], Fengting Xu [b,*], Ralph G. Nuzzo [a,c], Judith C. Yang [b]

[a] *Department of Chemistry, University of Illinois at Urbana-Champaign, Urbana, IL 61801, USA*
[b] *Department of Materials Science and Engineering, University of Pittsburgh, Pittsburgh, PA 15261, USA*
[c] *Department of Materials Science and Engineering, University of Illinois at Urbana-Champaign, Urbana, IL 61801, USA*

## Abstract

The structure of Au heterogeneous catalysts on the anatase form of TiO$_2$ has been characterized by high-resolution electron microscopy (HREM) and quantitative Z-contrast scanning transmission electron microscopy (STEM). These materials are prepared by deposition of highly monodisperse Au$_{13}$[PPh$_3$]$_4$[S(CH$_2$)$_{11}$CH$_3$]$_4$ (8-Å diameter) ligand-protected clusters on anatase, followed by reaction with ozone or a rapid oxidative thermal treatment to remove the ligands. The materials obtained differ markedly in each case. For the thermal treatment at 400 °C in air, the supported particles grow to an average size of 2.7 nm ($\pm$0.6 nm) in diameter, and the larger particles in the distribution are found to adopt a spherical geometry. Particle growth is greatly inhibited when ozone is used to remove the ligands (average diameter 1.2 $\pm$ 0.5 nm). These particles assume a more oblate geometry, consistent with a truncated hemispherical shape. It was found that subsequent thermal treatments of the ozone-derived supported nanoparticles at 400 °C in air did not induce additional growth, indicating that sintering is strongly affected by the particle–support interactions developed by the ozone-based low-temperature ligand removal step. These materials exhibit catalytic activity and high stability for the oxidation of CO at elevated temperatures, with the level of activity dependent on catalyst preparation.
© 2006 Elsevier Inc. All rights reserved.

*Keywords:* Au catalysis; HAADF-STEM; Electron microscopy; Cluster precursor

## 1. Introduction

The study of catalysis by gold, long thought to be a poor catalyst due to its nobility, has attracted increasing interest since the demonstration of low-temperature CO oxidation on metal-oxide-supported gold nanoparticles by Haruta et al. [1]. Since that time, the catalytic activity of gold has been recognized for a variety of reactions, including oxidation of propene to propene oxide, NO$_x$ reduction, selective hydrogenation of acetylene, and the water–gas shift reaction [2–4]. CO oxidation is the most extensively studied of these reactions. Despite this attention, the exact reaction mechanism and the nature of the catalytic site remains a subject of debate [3]. Whereas some studies have fo-

cused on Au$^0$ as the catalytic species, others have presented evidence of the active role of Au$^+$ or Au$^{3+}$ species [5–15]. In the cases where gold nanoparticles are determined to be the catalytically active species, their high activity has been postulated to be due to the large percentage of low-coordination surface Au atoms, the impact of size-dependent quantum effects on nanoparticle electronic properties, and/or the reactivity of the Au–support interface at the nanoparticle perimeter [2,4, 6,11–15].

Improved understanding of these catalysts via studies that systematically vary particle size or support identity is an obvious goal. This is difficult in practice, however, because access to a wide range in nanoparticle sizes in real-world catalysts is often achieved through use of different methods of preparation and that same preparation techniques are not suitable for all supports [4,14]. The activity of supported gold catalysts has been found to be highly dependent on preparation conditions,

making inferences about activity trends based solely on the end structure of the catalyst difficult [16].

Various techniques are commonly used to prepare supported gold catalysts. Deposition–precipitation consists of titrating $HAuCl_4$ solutions with a base to displace the chloride ions and form a gold hydroxide, followed by addition of a metal-oxide support [4]. With careful control of concentration, temperature, and pH, the $Au(OH)_3$ or $Au(OH)_4^-$ precipitates on the support, after which the material is fully washed to remove chloride and then calcined [4,17,18]. The efficient removal of $Cl^-$ is essential, because its presence during calcination has been found to induce sintering, leading to very large particles [4]. The main limitation of the deposition–precipitation technique is that it is not applicable to supports with low isoelectric points (e.g., $SiO_2$, $WO_3$, zeolites) or for carbon supports [3,4]. Particle sizes are typically in the range of 2–5 nm [19–21]. Some studies have also reported the presence of very large (5–20 nm) particles, possibly due to Au-hydroxyl precipitation in solution and deposition of larger precipitate crystals onto the support [22]. A second method of preparation is coprecipitation of Au precursors with metal hydroxides or carbonates to form the metal-oxide support and simultaneously deposit the Au precursor [4]. This technique generally produces catalysts with inferior activity to the deposition–precipitation method and the variety of accessible metal oxides is more restricted [23]. The deposition of monodisperse Au nanoparticles or colloids onto supports has also been studied [4,24–29]. Tsubota et al. found that high-temperature calcination (600 °C) was necessary to increase the activity of 5-nm gold colloids mixed with $TiO_2$ [24]. Although this increased particle sizes to 12 nm, it also resulted in greater contact between the Au particles and $TiO_2$ support [24]. The precise atomic scale characteristics of this more effective metal–support interaction remain unclear, however.

Smaller gold nanoparticle precursors have also been deposited on metal oxide supports. The smaller size and improved monodispersity of these nanoparticles is achieved by using strongly interacting surface species (e.g., dendrimers, oligomers, thiolates) as protecting ligands [29–31]. Therefore, to obtain catalytic activity, the ligands must be removed postdeposition [31]. This typically involves thermal treatments that result in nanoparticle growth and a loss of monodispersity, nullifying one main advantage of using such forms of nanoparticle precursors [25–27,29,31].

We present a protocol involving the deposition of a ligand-protected, subnanometer cluster, $Au_{13}[PPh_3]_4[S(CH_2)_{11}CH_3]_4$, onto a $TiO_2$ (anatase form) support. Ligand removal is achieved by flowing ozone over the supported clusters, a procedure that provides considerable advantages over thermally driven oxidative treatments. The products of these preparations are compared on the basis of their catalytic activity for the oxidation of carbon monoxide. The size and shape of the resulting supported nanoparticles are characterized using quantitative Z-contrast, high-angle annular dark-field scanning transmission electron microscopy (HAADF-STEM). High-resolution electron microscopy (HREM) is used to determine atomic-level characteristics of the nanoparticle structure. The characteristics of this synthetic methodology are discussed, as are the capabilities of the quantitative HAADF-STEM technique in comparison with other techniques commonly used in the structural characterization of catalysts.

## 2. Experimental

### 2.1. Cluster deposition

The ligand-protected Au cluster, $Au_{13}[PPh_3]_4[S(CH_2)_{11}CH_3]_4$, was synthesized as reported previously [32]. A 1-wt% Au on $TiO_2$ sample was prepared by dissolving the cluster (70 mg) in toluene (25 mL) and adding this solution to 4 g of $TiO_2$ (anatase, Fisher Scientific, 0.3 µm average particle size). This suspension was sonicated briefly and then stirred for 2 h. The supported clusters were collected on a medium glass frit, washed with toluene, and dried on the frit. The $TiO_2$-supported clusters were light brown in color. The actual loading of Au on $TiO_2$ was determined by evaporating the toluene from the filtrate and subtracting the mass of the undeposited cluster and was consistently found to be 0.8 wt% Au.

### 2.2. Ligand removal

Removal of the protecting ligands from the supported clusters was achieved by loading 1–2 g of the Au-loaded $TiO_2$ into a flow-through reactor cell. Ozone (0.15% in oxygen) from an ozone generator (Ozone Research and Equipment Corp.) was passed over the sample at a rate of 1 L/min for 1 h at room temperature. The ozone concentration was determined using a starch-iodide titration (standard method 408A) [33]. For the thermal treatments, the samples were annealed at 400 °C for 2 h in air, conditions found to be minimally sufficient to remove the ligands. The samples were placed into a furnace equilibrated at 400 °C, so that the heating rates were rapid.

### 2.3. Electron microscopy

The $TiO_2$-supported nanoparticles were suspended in acetone or toluene, and a drop of this suspension was deposited onto TEM grids bearing an ultrathin carbon film (Ted Pella, Inc.) and air-dried. HREM images were acquired using a field-emission JEM 2010F (S)TEM operated at 200 kV with an HREM point resolution of 2.4 Å or a JEM 2010 $LaB_6$ TEM operated at 200 kV with a point resolution of 2.8 Å. The quantitative HAADF-STEM experiments were performed on a field emission Vacuum Generators HB501 STEM operated at 100 kV with a probe size of 1 nm. The inner portion of the annular dark field detector was blocked with a mask such that the inner angle of detection was 110 mrad. Images were acquired at $1M\times$ magnification, and the image size was $1024 \times 1024$ pixels, yielding a pixel dimension of 0.62 Å. The electron beam current was measured with a Keithley analog electrometer capable of measuring pA currents, connected to one of the collector apertures. The details of detector calibration, determination of absolute intensity, and calculation of particle atom counts were reported

previously [32,34,35]. All image analyses were carried out using Gatan Digital Micrograph™ software. The intensities of the supported particles were measured by integrating the detector counts within a circle drawn around each particle (being careful not to truncate any intensity from the particle). The background signal (from support scattering and detector dark current) was taken as the average signal in an annulus around this boundary and was subtracted from each pixel within the boundary before integration. Particle diameters were determined from line profiles taken across individual particles. For each sample, 100 particles were analyzed to provide meaningful statistics. Only those Au particles that were imaged in the top view were analyzed; those particles imaged in profile at the edges of the $TiO_2$ particles were not used for the quantitative analysis. This was done to minimize errors in the diameter measurements used to determine nanoparticle shape via atom count–diameter correlations.

## 2.4. Measurements of catalytic performance

Conversion–temperature plots, also known as light-off curves, were collected for the CO oxidation reaction in a single-pass glass reactor. Reactions were performed at atmospheric pressure and with a space velocity of 3000 mL/(h g catalyst) [375,000 mL/(h g Au)]. The temperature was varied between 30 and 450 °C using a furnace to heat the reactor isothermally. The reaction feed was composed of 2% CO and 8% $O_2$, balanced with He. The reaction products were analyzed using gas chromatography (GC) with mass spectrometric detection (Agilent 6890/5973 GC-MS). The GC column was an Agilent GS-CarbonPLOT (with a bonded, monolithic carbon-layer stationary phase) capillary column (30 m long, 0.32 mm i.d.).

## 3. Results

### 3.1. HAADF-STEM

Z-contrast microscopy (where Z refers to the atomic number) is a powerful technique that is particularly well suited for characterizing high-Z metal catalysts supported on low-Z supports [36–38]. The technique is a mode of detection in STEM in which the electrons scattered by the sample are collected at large angles with an inner angle of detection typically >90 mrad [34]. At these high angles, electron scattering is largely incoherent Rutherford scattering, and contributions from Bragg diffracted electrons are minimal [37]. Because the cross-sections for Rutherford scattering are proportional to $Z^2$, metal nanoparticles appear as bright spots on a lower Z support [35,37]. In addition, the scattering intensity is directly proportional to the number of atoms in the particle, and as a result, the measured intensities can be quantitatively correlated to the number of atoms in the cluster or nanoparticle given proper calibration of the detector efficiency and theoretical calculation of the electron scattering cross-section over the scattering angles measured [32,34,35,39]. For the Au nanoparticles studied in this report, the theoretical scattering cross-section is calculated for single-scattering of electrons only. This is justified

given that for Au, the total mean free path (elastic and inelastic scattering) is ca. 8 nm for 100-keV electrons, and the largest nanoparticles imaged in this work have diameters not exceeding 4 nm [40]. As a result, plural scattering is negligible.

Representative HAADF-STEM images are presented of the $Au_{13}$ clusters deposited on $TiO_2$ before ligand removal (Fig. 1a) and of the Au nanoparticles with ligands removed using the thermal treatment (Fig. 1b) or ozone treatment (Fig. 1c). For the deposited ligand-protected clusters, it is evident that there are some larger Au gold particles, although these are a minority species. (We cannot discount electron-beam-induced damage as a source of these larger clusters.) The vast majority of the deposited clusters have diameters consistent with $Au_{13}$ cores (0.8 nm) [32]. These larger particles may be present as impurities in the $Au_{13}$ cluster solution before deposition on the support or could result from sintering events during the deposition process [32]. Extended X-ray absorption fine structure (EXAFS) measurements on these deposited clusters indicate that there is no significant change to the cluster structure, that is, decomposition or agglomeration [41].

The calcination of the deposited ligand-protected clusters at 400 °C results in particle growth, to an average diameter of $2.7 \pm 0.6$ nm ($\pm 23\%$). The edge profiles shown in Fig. 1b (i.e., particles viewed side-on at the edge of the $TiO_2$ support) suggest a nearly spherical shape for the larger Au nanoparticles, an inference supported by further analysis of the HAADF-STEM and HREM images (see below). The size of these supported particles is similar to that of materials prepared using the deposition–precipitation method described in the literature [19–21].

The removal of ligands from the deposited clusters via a reaction with ozone yields supported nanoparticles that are much smaller (Fig. 1c), with an average diameter of $1.2 \pm 0.5$ nm ($\pm 40\%$). The removal of ligands was independently confirmed by the loss of Au-"low Z" scattering contributions in EXAFS spectra and by the loss of S and P peaks in X-ray photoelectron spectra (XPS) [41]. Both XPS and EXAFS data indicate that the gold nanoparticles are fully reduced to $Au^0$ [41]. Similar reactive oxygen treatments have been used to remove ligands from gold nanoparticles, but, to the best of our knowledge, the use of this method for preparing ligand-free nanoparticles on catalyst supports is limited to the study of Cuenya et al. investigating the electrocatalytic activity of $O_2$-plasma-treated Au nanoparticles on a two-dimensional indium tin oxide support [42–46].

The strong Au–$TiO_2$ interaction for this ozone-treated sample is indicated by the fact that calcination at 400 °C results in only slight growth in particle size (Fig. 1d) to $1.5 \pm 0.4$ nm ($\pm 23\%$). Contrasting this with the calcination of the ligand-protected clusters clearly shows that the strongly anchored Au nanoparticles are much more resistant to sintering than the more mobile clusters.

The distribution of particle sizes and atom counts determined using the quantitative HAADF-STEM technique are presented in histogram form in Fig. 2 for the three samples of ligand-free nanoparticles. The average number of atoms per nanoparticle was 324 for the thermally treated sample, 40 for the ozone-treated sample, and 46 for the ozone-calcined sample. The fact
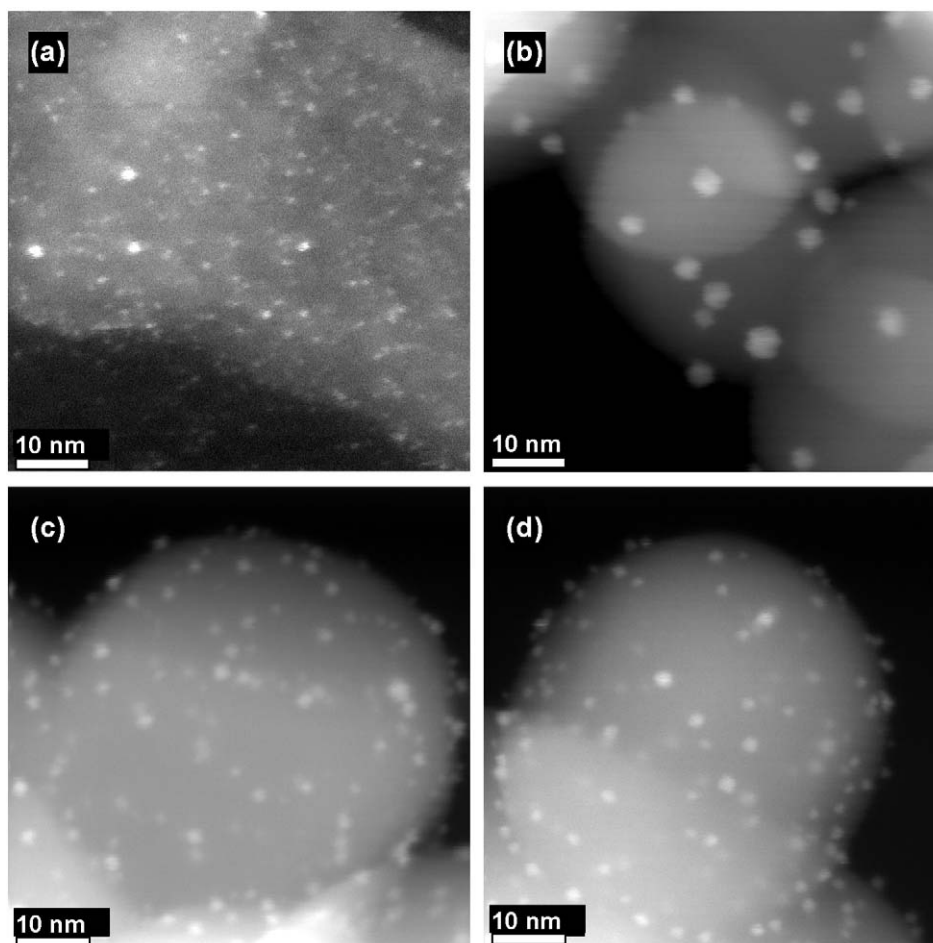
Fig. 1. Representative HAADF-STEM images of (a) Au$_{13}$ clusters deposited on anatase support, (b) nanoparticles after thermal treatment, (c) nanoparticles after ozone treatment, and (d) nanoparticles after ozone treatment followed by calcination.

that the average number of atoms per nanoparticle increased only slightly after calcination in the case of the ozone-treated sample while the average measured diameter increased more significantly suggests a change in nanoparticle morphology on calcination to a more oblate shape (i.e., an increase in surface wetting) [35]. The HAADF-STEM data discussed below support this conclusion.

Because the HAADF-STEM signal is due to incoherent scattering and is proportional to the number of atoms in the nanoparticle, the relationship between the measured intensity and the particle diameter is characteristic of the particle's shape [32,35,37,47]. Comparing the relative intensities as a function of nanoparticle diameter can provide insight into the nature of nanoparticle growth [37,47]. If the intensity varies linearly with $d^3$ (where $d$ is the particle diameter) then the particles grow three-dimensionally (e.g., growth of spheres or hemispheres with constant aspect ratio) [35,37,47]. But if the intensity varies linearly with $d^2$, then the particles grow two-dimensionally (monolayer, bilayer, etc. rafts), maintaining a constant height [35,37,47]. Extrapolating information about nanoparticle growth from these relative intensity measurements to the actual particle shape, however, requires additional information (e.g., from EXAFS or HREM) or assumptions, because any shape that grows with a constant height or a constant

aspect ratio will show relative intensities with a $d^2$- or a $d^3$-dependence, respectively [35,47]. But this is not the case if the absolute intensities (or, equivalently, the calculated atom counts) are used for a similar analysis [32,35]. Fig. 3 displays the atom count for each individual supported nanoparticle plotted as a function of its diameter for the thermally treated, ozone-treated, and ozone-calcined samples. The data are plotted with the calculated values for monolayer and bilayer rafts, truncated cuboctahedra [(111) basal plane, hemispherical truncation], and cuboctahedra. These latter two models represent hemispherical and spherical shapes, respectively, that are consistent with a Wulff construction in which surface energy is reduced by minimization of high-index surface planes [48]. These plots present the full distribution of data in a convenient format. However, some caution is warranted in their interpretation when they are used to describe nanoparticles with a broad size distribution. Although an assumption of similar morphologies over a small range of supported nanoparticle sizes may be warranted, there is a greater likelihood that this will not hold over larger size distributions. For example, the largest supported Au nanoparticles for a given catalyst sample may preferentially exhibit a spherical shape, whereas smaller nanoparticles in the same sample assume more oblate morphologies. A more rigorous statistical analysis over smaller particle diameter ranges is use-

### Au on TiO$_2$ – Thermal Treatment



### Au on TiO$_2$ – Ozone Treatment



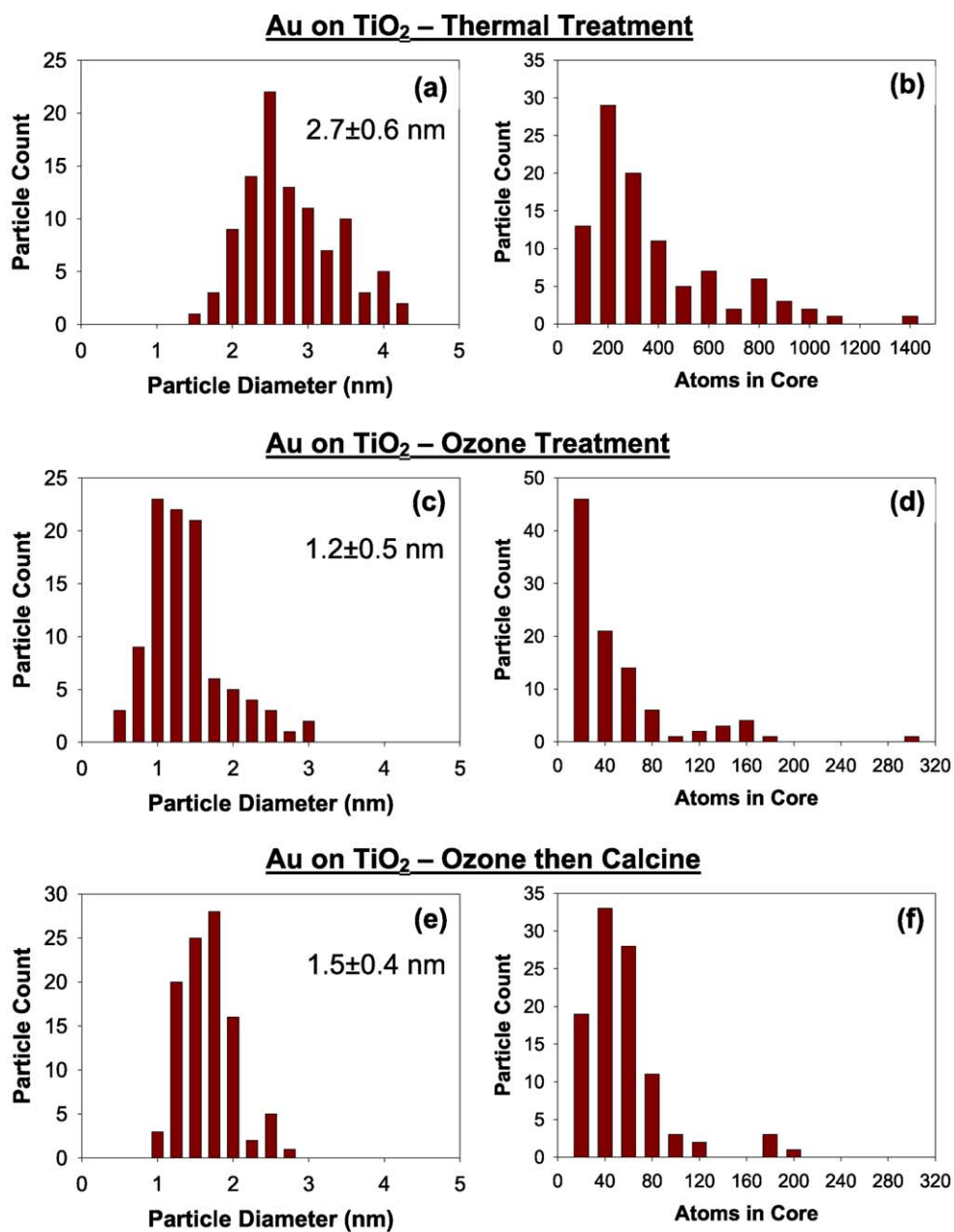### Au on TiO$_2$ – Ozone then Calcine



Fig. 2. Distribution of particle diameters and atom counts for (a,b) nanoparticles after thermal treatment, (c,d) nanoparticles after ozone treatment, and (e,f) nanoparticles after ozone treatment followed by calcination.

ful in describing any size-dependent evolution in nanoparticle shape.

Inspection of the intensity–diameter data for the thermally-treated nanoparticles (Fig. 3a) shows that the smallest particles in the distribution assume a hemispherical shape with an evolution to more spherical nanoparticles at larger diameters. To better evaluate this behavior, the variance between the experimental data and each model is calculated over a more limited range of nanoparticle sizes. The confidence levels that the lower variance of the best-fitting model is statistically significant are estimated using an F-test and are reported in Table 1 [49]. In accordance with the conclusions drawn from inspection of Fig. 3a, it is apparent that the smallest nanoparticles present in the thermally treated samples are best described by the truncated

cuboctahedral model. At larger sizes, the nanoparticles assume a more spherical shape. The conclusion about morphology for the larger-diameter particles is consistent with the observation of seemingly spherical particles with large Au–TiO$_2$ contact angles observed in profile in the HAADF-STEM images. We note, however, that the distribution of data is asymmetric and lies to the right of the cuboctahedral model, indicating that the particles are somewhat truncated, albeit not to an extent as to be better described as hemispherical. This conclusion is supported by HREM of these thermally treated nanoparticles (see below).

This morphology contrasts with that of the smaller supported nanoparticles prepared by ozone treatment of the cluster precursors (Fig. 3b). It is difficult to assign a single model that best
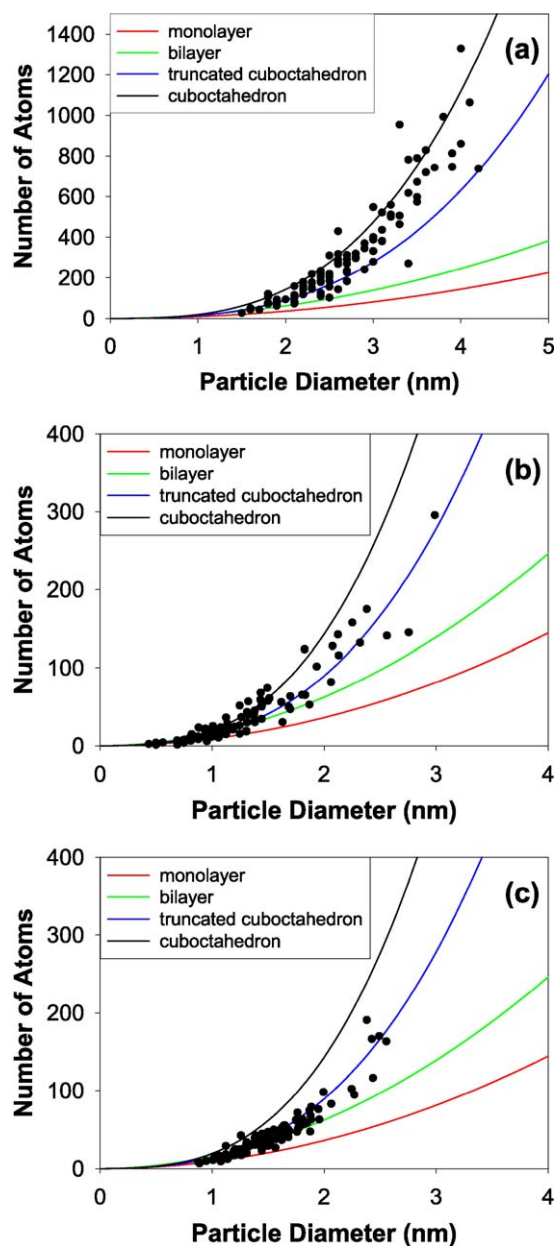
Fig. 3. Number of atoms in the Au nanoparticles plotted as a function of nanoparticle size for (a) nanoparticles after thermal treatment, (b) nanoparticles after ozone treatment, and (c) nanoparticles after ozone treatment followed by calcination.

describes the shape of the subnanometer clusters in this sample. In this size range, the models converge. In addition, for nanoparticles of this size, there is a greater uncertainty in determining the nanoparticle diameter, particularly given the finite size of the electron probe, which has the effect of smearing the nanoparticle boundary [39]. We note that a definitive assignment of spherical shape was possible for the highly monodisperse 0.8-Å $Au_{13}$ clusters supported on a very-low-contrast carbon film [32]. In the present study, however, the compounding effect of a real distribution of particle sizes makes such an assignment difficult. At slightly larger sizes (1.0–1.5 nm), the clusters agree best with a cuboctahedral model, although there is considerable overlap with the truncated cuboctahedral model.

Table 1
Best-fit models of supported nanoparticle shape

| Data range (nm) | No. particles | Best model | Confidence over other models (%) |
|---|---|---|---|
| Au on TiO$_2$—thermal treatment | | | |
| 1.5–2.5 | 42 | T | 99 (C),100 (B), 100 (M) |
| 2.5–3.5 | 44 | C | 83 (T), 100 (B), 100 (M) |
| 3.5–4.2 | 14 | C | 84 (T), 98 (B), 99 (M) |
| Au on TiO$_2$—ozone treatment | | | |
| 0–1.0 | 34 | C | 14 (T), 27 (B), 92 (M) |
| 1.0–1.5 | 43 | C | 51 (T), 91 (B), 100 (M) |
| 1.5–3.0 | 23 | T | 100 (T), 100 (B), 100 (M) |
| Au on TiO$_2$—ozone then calcine | | | |
| 0–1.0 | 3 | | |
| 1.0–1.5 | 42 | T | 15 (B), 100 (C), 100 (M) |
| 1.5–3.0 | 55 | T | 100 (C), 100 (B), 100 (M) |

C = cuboctahedron, T = truncated cuboctahedron, B = bilayer, M = monolayer.

Finally, for the larger nanoparticles in the sample (1.5–3.0 nm), the nanoparticles assume a truncated cuboctahedral morphology. On calcination (Fig. 3c), the data are best fit by the truncated cuboctahedral model across the full data range, and there are two obvious changes in the distribution. First, calcining the sample results in the loss of the smallest nanoparticles, those with diameters < 1 nm. Second, the thermal treatment results in a flattening of the nanoparticles, as was suggested above. For the smaller nanoparticles in the distribution (<1.5 nm), it is difficult to distinguish between a truncated cuboctahedral and a bilayer raft shape.

### 3.2. HREM

Representative HREM images of the thermally treated and ozone-treated samples are shown in Fig. 4. The larger nanoparticles seen in the sample in which ligand removal was achieved thermally appear as rounded particles with relatively small contact areas with the TiO$_2$ support. The particle shown in Fig. 4a has an aspect ratio (particle height/diameter) of approximately 0.85, which is representative of the larger particles in this sample. The particles with ligands removed via ozone treatment (Fig. 4b) appear to have greater contact with the support and appear as truncated cuboctahedra, as indicated by the HAADF-STEM analysis. They exhibit faceted surfaces, in contrast to the rounded thermally treated particles. We note that the particles represented in Fig. 4 have diameters consistent with the largest sizes observed in the supported nanoparticle samples. Thus, although shape determination is fairly easy from the HREM images for these particles, the HAADF-STEM technique is more accurate for nanoparticles containing <100 atoms [35]. As indicated by the inset Fourier transforms of the gold nanoparticles, supported nanoparticles prepared by either thermal or ozone treatment exhibit a face-centered cubic structure. This indicates an evolution in nanoparticle structure on loss of ligands and sintering from the icosahedral structure of the $Au_{13}$ precursor cluster [50]. Finally, we note the presence of dynamical structural changes under the electron beam, as has been well documented in the literature [51,52]. We generally observed a flattening of the Au nanoparticles on prolonged exposure (minutes) in the
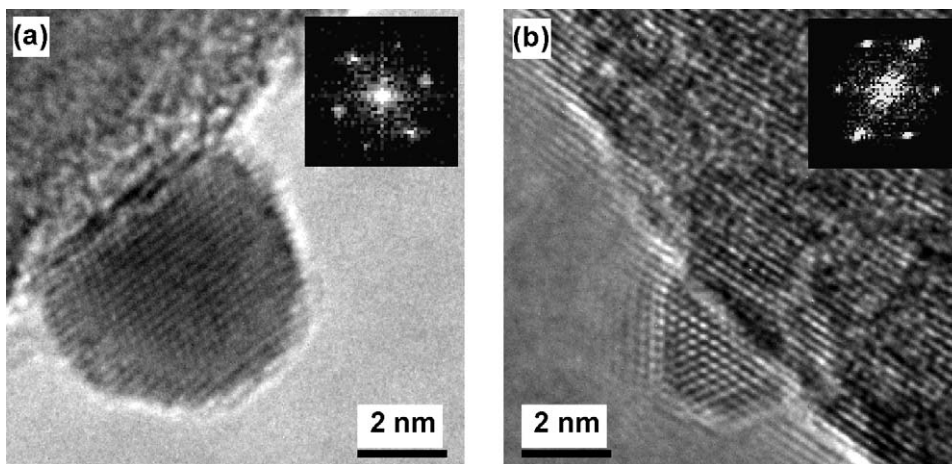
Fig. 4. HREM images of a Au nanoparticles on $TiO_2$ support after ligand removal by (a) thermal treatment and (b) ozone treatment. The insets are the Fourier transforms of the Au particles, indicating face-centered cubic structure.
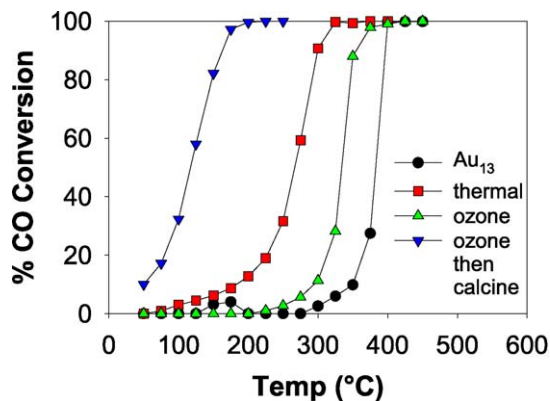


Fig. 5. Light-off curves characterizing the oxidation of CO as a function of temperature over $Au_{13}$ ligand-protected clusters on anatase and over Au nanoparticles prepared by ligand removal using ozone treatment, thermal treatment, and ozone treatment followed by calcination.

electron beam. The images in Fig. 4 and the larger dataset of which they are representative were acquired as quickly as possible, to minimize the contribution of such beam-driven dynamics and their impact on the conclusions regarding nanoparticle shape.

### 3.3. Catalytic performance

The light-off curves of the oxidation of CO for the parent $Au_{13}$ clusters supported on $TiO_2$ and for the three catalysts prepared by ligand removal are presented in Fig. 5. For the $Au_{13}$ clusters on $TiO_2$, the slight increase in activity at 150 °C is non-catalytic and occurs at the temperature at which the thermal loss of ligands begins, as determined by thermogravimetric analysis (TGA); see Supplementary Material. Catalytic activity does not begin until the temperature exceeds 300 °C. TGA indicates that the loss of the protecting ligands is virtually complete at this temperature, confirming that ligand removal is necessary for catalytic activity. The Au catalyst undergoing ozone treatment exhibits higher activity, with the temperature at which 50% conversion occurs ($T_{50}$) of 335 °C. The calcination of this ozone-treated sample resulted in a substantial increase in activ-

ity ($T_{50} = 115$ °C). The catalyst prepared using only the thermal treatment achieved 50% conversion at 265 °C. All of the catalysts showed good thermal stability, with no loss in activity after remaining under a continuous flow of reactants at 450 °C for several hours, as confirmed by measurements made on returning to a lower temperature at which conversion was <100%. A control experiment performed on the bare anatase support showed minimal conversion (5%) at 450 °C.

### 4. Discussion

Use of the $Au_{13}[PPh_3]_4[S(CH_2)_{11}CH_3]_4$ cluster as a precursor for the supported Au nanoparticles appears to have several advantages. First is the ability to prepare supported particles with a small average size and narrow size distribution. Even on thermal ligand removal, the size and distribution of nanoparticles are similar to those of Au nanoparticles derived from $Au^{3+}$ precursors, and the average size is smaller than catalysts derived from nanoparticles covered with higher-molecular-weight, lower-volatility protecting species (oligomers, dendrimers) [19–21,25–27,29,31]. When a $Pt_2Au_4$ cluster protected with the highly volatile ligand, *tert*-butylacetylene, was used as a precursor, then calcined, the average diameter of the resulting nanoparticles was 1.2 nm [28]; however, monometallic Au clusters protected by such low-molecular-weight ligands are not available, and the presence of Pt in the bimetallic precursor may help prevent sintering due to platinum's greater affinity for metal oxides [4].

The use of ozone for ligand removal results in 1.2-nm diameter $Au^0$ nanoparticles, smaller than those obtainable using other preparation methods, expanding the range of nanoparticle sizes that can be investigated in size–activity studies [4]. These ozone-treated nanoparticles are characterized by a strong Au–$TiO_2$ interaction (a prerequisite for high catalytic activity), as evidenced by their truncated shape and resistance to sintering on calcination at 400 °C [53]. The surface wetting of the nanoparticles is even greater after calcination of the ozone-treated nanoparticles, resulting in flattening of the nanoparticles. Interestingly, Yan et al. found the loss of similar high-

catalytic raftlike structures on heating to 300 °C, whereas the particles prepared from the $Au_{13}$ cluster precursors appear quite stable at temperatures up to 400 °C [22]. The difference in the impact of thermal treatment on the ligand-protected clusters and the ozone-treated nanoparticles indicates the very different environments in which sintering proceeds. For the ligand-protected clusters, the growth behavior is consistent with significant mobility of the clusters on the support and the lability of the phosphine and thiolate ligands at high temperature [3,53]. The moderate annealing of thiolate-protected gold nanoparticles at temperatures below the boiling point of the protecting thiolates is known and has been used to achieve controlled growth [54]. The calcination temperature used was 400 °C, which is above the boiling point for both the triphenylphosphine (∼375 °C) and dodecanethiol (∼275 °C) ligands. The rate of heating to the calcination temperature, a parameter not explored in the current work, may strongly affect the end nanoparticle size by increasing the time at which the samples are at high temperature but have not undergone ligand volatilization. The ozone-treated sample consists of nanoparticles that are strongly anchored to the support and also lack the organic ligands to act as a solvent in a solution-phase annealing process. As a result, they exhibit considerable resistance to sintering.

The deposition of $Au_{13}[PPh_3]_4[S(CH_2)_{11}CH_3]_4$ is the result of adsorption of the cluster on the support and not of impregnation; the volumes used for the deposition solution are much greater than the pore volume of the support, and the supported clusters are thoroughly washed with solvent after deposition. Further studies have indicated that adsorption of these $Au_{13}$ clusters can be achieved on a range of high-surface area supports, including carbon and $SiO_2$ at loadings > 1 wt% Au—an advantage over deposition–precipitation methods [41]. In the case of $TiO_2$, the observed loading limit of 0.8 wt% Au can be increased by using a higher-surface area $TiO_2$ support.

The activity observed in the light-off curves confirms that these materials are catalysts for the oxidation of CO. The conversion temperature studies are valuable for activity comparisons across catalyst samples measured under the same operating conditions [55]. We note that the dramatic increase in activity for the ozone-treated sample on calcination may result from the flattening of the nanoparticles (increased particle–support interface) or from the burning off of residue that was not fully removed during the ozone treatment [24]. Also of note is the significantly higher activity for the smaller Au nanoparticles (avg. 46 atoms) prepared by ozone treatment followed by calcination compared with that for the larger nanoparticles (avg. 324 atoms) of the catalyst prepared using solely the thermal treatment. This observation is in agreement with studies suggesting that increasing activity with decreasing nanoparticle size is a trend that holds for nanoparticles as small as 1 nm, and in contrast to studies on a model $Au–TiO_2(001)–Mo(100)$ system indicating that maximum activity occurs for 3-nm nanoparticles with decreasing activity at smaller and larger sizes [6,17,22].

Comparing light-off curves collected under different operating conditions is difficult, because the observed conversion is impacted not only by the inherent reaction rate, but also by mass transfer phenomena [55]. These contributing phenom-

ena are not easily or unambiguously decoupled [55]. We note that the support used in the present work was a low-surface area $TiO_2$. Recent studies have indicated increased activity for metal-oxide-supported Au nanoparticles with increasing support surface area [56,57]. This is an impact that can be readily studied in future work given the general applicability of the synthesis protocol across different supports. Finally, catalyst deactivation in oxidative environments is a key issue in catalysis by supported Au nanoparticles [58,59]. One cause of this deactivation is believed to be the sintering of the Au nanoparticles [58]. In this regard, the remarkable thermal stability of the cluster-derived catalysts at temperatures up to 450 °C, as evidenced by both the catalytic activity and the electron activity, is of particular interest.

We turn now to a discussion regarding the characterization of these catalysts. A number of experimental techniques are used for the size determination of heterogeneous catalysts composed of metal nanoparticles on a support, including XRD, small angle X-ray scattering (SAXS), EXAFS, and electron microscopy [60]. Nanoparticle size is estimated from X-ray diffractograms using Scherrer's equation to fit the broadened diffraction peaks [61,62]; however, this approach is difficult for the smallest particles (<2 nm), because of the extensive peak broadening [26]. SAXS has proven useful for determining nanoparticle size in two-phase systems (e.g., particles in air, solution, or films) [63]; however, nanoparticles supported on a porous support represent a three-component sample consisting of the support, pores, and metal nanoparticles [60]. Therefore, fitting the scattering data requires the difficult fitting (or subtraction) of the various scattering contributions with form factors correctly modeled for the pore and nanoparticle geometries and size distributions [60]. EXAFS can be used to determine nanoparticle size from the measured coordination numbers [17,64]. But this requires knowledge of the nanoparticle shape, either by using a complementary characterization technique such as TEM or by analyzing the coordination numbers from multiple scattering shells concurrently [17,47,50,64]. Coordination numbers are sensitive to nanoparticle size for particles <5 nm in diameter, but for larger particles, the variation in coordination number is less sensitive and asymptotically approaches the bulk value [17,64]. In addition, EXAFS is an ensemble technique and as such should be verified using electron microscopy to ensure that the average diameter determined from the ensemble describes a relatively narrow distribution of particles and is not, say, an average between a population of monoatomic species and large bulk-like particles.

Given the potential pitfalls of the techniques discussed above, electron microscopy is often used as a complementary technique to verify the particle size characterization by scattering or diffraction methods. The corollary to this is that the ensemble scattering and diffraction techniques are used to verify that the microscopically determined particle distributions are representative of the sample. For the smallest particle sizes, accurately counting particles using conventional TEM or bright-field STEM is difficult due to the poor contrast between particles and support [32,36]. The use of HAADF-STEM provides much greater contrast between the particles and the

support and enables imaging down to the level of single metal atoms on supports [32,34,35,38,39,65]. An additional advantage of HAADF-STEM is the ability to determine nanoparticle shape from two-dimensional images by analyzing the dependence of scattering intensity on the particle diameters [32,35, 37,47]. Whether the particles grow three-dimensionally or two-dimensionally can be determined even for the case in which the relative scattering intensities are used, although the exact determination of the nanoparticle shape requires information from additional characterization techniques [37,47]. The use of absolute, calibrated scattering intensities or atom counts in such an analysis precludes the need for a secondary technique to calibrate the particle shape determination and thus provides an explicit and general technique that can be used to determine the shape of nanoparticles, here for Au on $TiO_2$ [32,35].

## 5. Conclusion

The use of the cluster molecule $Au_{13}[PPh_3]_4[S(CH_2)_{11}$-$CH_3]_4$ has been demonstrated for the preparation of bare Au nanoparticles supported on $TiO_2$. Ligand removal was achieved by either thermal or ozone treatment. For the thermally treated nanoparticles, particle growth was modest (increase in average diameter from 0.8 to 2.7 nm), and particles $< 2.5$ nm had a hemispherical geometry evolving with increasing particle size to a spherical geometry with a support interaction characterized by a large contact angle. The ozone-treated sample displayed a mean diameter of 1.2 nm, significantly smaller than that reported for other preparation methods currently available. These particles proved to be resistant to further sintering at 400 °C. The catalysts thus prepared demonstrated activity for the oxidation of CO at elevated temperature and good stability. This method of catalyst preparation is well suited to studies investigating the relationship between particle size and catalytic activity, as well as the contribution of the support to activity. The use of quantitative HAADF-STEM is a powerful technique for characterizing nanoparticle size and shape.

## Supplementary material

Supplementary material for this article may be found on ScienceDirect, in the online version.

Please visit DOI:10.1016/j.jcat.2006.07.006

## References

[1] M. Haruta, N. Yamada, T. Kobayashi, S. Iijima, J. Catal. 115 (1989) 301.
[2] M. Haruta, Chem. Record 3 (2003) 75.
[3] R. Meyer, C. Lemire, S.K. Shaikhutdinov, H.-J. Freund, Gold Bull. 37 (2004) 72.
[4] M. Haruta, Gold Bull. 37 (2003) 27.
[5] G.J. Hutchings, Gold Bull. 37 (2003) 3.
[6] M. Valden, X. Lai, D.W. Goodman, Science 281 (1998) 1647.
[7] S. Minico, S. Scire, C.D. Crisafulli, A.M. Visco, S. Galvagno, Catal. Lett. 47 (1997) 273.
[8] A.M. Visco, F. Neri, G. Neri, A. Donato, C. Milone, S. Galvagno, Phys. Chem. Chem. Phys. 1 (1999) 2869.
[9] E.D. Park, J.S. Lee, J. Catal. 186 (1999) 1.
[10] J. Guzman, B.C. Gates, Angew. Chem. Int. Ed. 42 (2003) 690.
[11] Z.-P. Liu, P. Hu, A. Alavi, J. Am. Chem. Soc. 124 (2002) 14770.
[12] N. Lopez, J.K. Norskov, J. Am. Chem. Soc. 124 (2002) 11262.
[13] C. Mohr, H. Hofmeister, J. Radnik, P. Claus, J. Am. Chem. Soc. 125 (2003) 1905.
[14] P. Claus, A. Bruckner, C. Mohr, H. Hofmeister, J. Am. Chem. Soc. 122 (2000) 11430.
[15] L.M. Molina, B. Hammer, Phys. Rev. Lett. 90 (2003) 206102.
[16] G.R. Bamwenda, S. Tsubota, T. Nakamura, M. Haruta, Catal. Lett. 44 (1997) 83.
[17] V. Schwartz, D.R. Mullins, W. Yan, B. Chen, S. Dai, S.H. Overbury, J. Phys. Chem. B 108 (2004) 15782.
[18] F. Moreau, G.C. Bond, A.O. Taylor, J. Catal. 231 (2005) 105.
[19] F.-W. Chang, H.-Y. Yu, L.S. Roselin, H.C. Yang, Appl. Catal. A 290 (2005) 138.
[20] R.J.H. Grisel, P.J. Kooyman, B.E. Nieuwenhuys, J. Catal. 191 (2000) 430.
[21] B.S. Uphade, T. Akita, T. Nakamura, M. Haruta, J. Catal. 209 (2002) 331.
[22] W. Yan, B. Chen, S.M. Mahurin, V. Schwartz, D.R. Mullins, A.R. Lupini, S.J. Pennycook, S. Dai, S.H. Overbury, J. Phys. Chem. B 109 (2005) 10676.
[23] R. Zanella, S. Giorgio, C.R. Henry, C. Louis, J. Phys. Chem. B 106 (2002) 7634.
[24] S. Tsubota, T. Nakamura, K. Tanaka, M. Haruta, Catal. Lett. 56 (1998) 131.
[25] K. Sayo, S. Deki, S. Hayashi, J. Mater. Chem. 9 (1999) 937.
[26] J.-D. Grunwaldt, C. Kiener, C. Wogerbauer, A. Baiker, J. Catal. 181 (1999) 223.
[27] J. Chou, N.R. Franklin, S.-H. Baeck, T.F. Jaramillo, E.W. McFarland, Catal. Lett. 95 (2004) 107.
[28] L.B. Ortiz-Soto, O.S. Alexeev, M.D. Amiridis, Langmuir 22 (2006) 3112.
[29] R.W.J. Scott, O.M. Wilson, R.M. Crooks, Chem. Mater. 16 (2004) 5682.
[30] A.C. Templeton, W.P. Wuelfing, R.W. Murray, Acc. Chem. Res. 33 (2000) 27.
[31] H.H. Kung, M.C. Kung, Top. Catal. 34 (2005) 77.
[32] L.D. Menard, S.-P. Gao, H. Xu, R.D. Twesten, A.S. Harper, Y. Song, G. Wang, A.D. Douglas, J.C. Yang, A.I. Frenkel, R.G. Nuzzo, R.W. Murray, J. Phys. Chem. B 110 (2006) 12874.
[33] Standard Methods for the Examination of Water and Wastewater, APHA, AWWA, WPCF, Washington, DC, 1981, p. 280.
[34] A. Singhal, J.C. Yang, J.M. Gibson, Ultramicroscopy 67 (1997) 191.
[35] J.C. Yang, S. Bradley, J.M. Gibson, Mater. Charact. 51 (2003) 101.
[36] J. Liu, Microsc. Microanal. 10 (2004) 55.
[37] M.M.J. Treacy, S.B. Rice, J. Microsc. 156 (1989) 211.
[38] P.D. Nellist, S.J. Pennycook, Science 274 (1996) 413.
[39] J.C. Yang, S. Bradley, J.M. Gibson, Microsc. Microanal. 6 (2000) 353.
[40] M.A. Khakoo, D. Roundy, C. Hicks, N. Margolis, E. Yeung, A.W. Ross, T.J. Gay, Phys. Rev. A 64 (2001) 052713.
[41] L.D. Menard, F. Xu, A.I. Frenkel, J.C. Yang, R.G. Nuzzo, in preparation.
[42] H.-G. Boyen, G. Kastle, F. Weigl, B. Koslowski, C. Dietrich, P. Ziemann, J.P. Spatz, S. Riethmuller, C. Hartmann, M. Moller, G. Schmid, M.G. Garnier, P. Oelhafen, Science 297 (2002) 1533.
[43] S. Chen, Langmuir 17 (2001) 2878.
[44] S. Pang, Y. Kurosawa, T. Kondo, T. Kawai, Chem. Lett. 34 (2005) 544.
[45] S.D. Pucket, J.A. Heuser, J.D. Keith, W.U. Spendel, G.E. Pacey, Talanta 66 (2005) 1242.

[46] B.R. Cuenya, S.-H. Baeck, T.F. Jaramillo, E.W. McFarland, J. Am. Chem. Soc. 125 (2003) 12928.

[47] A. Carlsson, A. Puig-Molina, T.V.W. Janssens, J. Phys. Chem. B 110 (2006) 5286.

[48] A.S. Barnard, X.M. Lin, L.A. Curtiss, J. Phys. Chem. B 109 (2005) 24465.

[49] R.M. Bethea, B.S. Duran, T.L. Boullion, Statistical Methods for Engineers and Scientists, Dekker, New York, 1975, p. 196.

[50] L.D. Menard, H. Xu, S.-P. Gao, R.D. Twesten, A.S. Harper, Y. Song, G. Wang, A.D. Douglas, J.C. Yang, A.I. Frenkel, R.W. Murray, R.G. Nuzzo, J. Phys. Chem. B 110 (2006) 14564.

[51] N. Doraiswamy, L.D. Marks, Surf. Sci. 348 (1996) L67.

[52] T. Akita, M. Okumura, K. Tanaka, M. Kohyama, M. Haruta, J. Mater. Sci. 40 (2005) 3101.

[53] M. Haruta, Catal. Today 36 (1997) 153.

[54] T. Shimizu, T. Teranishi, S. Hasegawa, M. Miyake, J. Phys. Chem. B 107 (2003) 2719.

[55] F. Duprat, Chem. Eng. Sci. 57 (2002) 901.

[56] J. Guzman, S. Carrettin, J.C. Fierro-Gonzalez, Y. Hao, B.C. Gates, A. Corma, Angew. Chem. Int. Ed. 44 (2005) 4778.

[57] J. Guzman, A. Corma, Chem. Commun. (2005) 743.

[58] T.V. Choudhary, D.W. Goodman, Top. Catal. 21 (2002) 25.

[59] W. Yan, S.M. Mahurin, Z. Pan, S.H. Overbury, S. Dai, J. Am. Chem. Soc. 127 (2005) 10480.

[60] B. Imelik, J.C. Vedrine (Eds.), Catalyst Characterization: Physical Techniques for Solid Materials, Plenum, New York, 1994.

[61] P. Scherrer, Gott. Nachr. 2 (1918) 98.

[62] H.P. Klug, L.E. Alexander, X-Ray Diffraction Procedures for Polycrystalline and Amorphous Materials, Wiley, New York, 1974.

[63] H. Borchert, E.V. Shevchenko, A. Robert, I. Mekis, A. Kornowski, G. Grubel, H. Weller, Langmuir 21 (2005) 1931.

[64] A.I. Frenkel, C.W. Hills, R.G. Nuzzo, J. Phys. Chem. B 105 (2001) 12689.

[65] K. Sohlberg, S. Rashkeev, A.Y. Borisevich, S.J. Pennycook, S.T. Pantelides, Chem. Phys. Chem. 5 (2004) 1893.